Optics Communications 495 (2021) 127073

Contents lists available at ScienceDirect

Optics Communications

journal homepage: www.elsevier.com/locate/optcom

Hybrid communication assisted by coherent oscillator using resonant excitation of Nitrogen–vacancy center in diamond

Faisal Nadeem [a], Faizan Raza [a], Kangkang Li [a], Huanrong Fan [a], Irfan Ahmed [b,c,*], Changbiao Li [a], Yanpeng Zhang [a,*]

[a] Key Laboratory for Physical Electronics and Devices of the Ministry of Education & Shaanxi Key Lab of Information Photonic Technique, Xi'an Jiaotong University, Xi'an 710049, China

[b] Department of Physics, City University of Hong Kong, Kowloon, Hong Kong

[c] Electrical Engineering Department, Sukkur IBA University, Airport Road, Sukkur 65200, Pakistan

ARTICLE INFO

Keywords:
Coherent oscillator
Hybrid communication
Nitrogen–vacancy center in diamond

ABSTRACT

We propose the multi-channel hybrid communication assisted by a coherent oscillator, by configuring the diamond Nitrogen–vacancy center using spontaneous parametric four-wave mixing. For one-channel hybrid communication, composite signal of fluorescence (information) and Stokes (carrier) is sent to the receiver; information is recovered by subtracting intensities of composite signal and reference coherent signal (from coherent oscillator) at demodulator. Further, we achieved two-channel and three-channel hybrid communication through two-mode and three-mode intensity–noise correlation, respectively. Two-mode correlation of hybrid signal (produced through photon subtraction) and anti-Stokes demonstrates the nonclassical behavior by violating Cauchy–Schwarz inequality, verified through corresponding squeezing (−5 dB). Such phenomenon of non-classical behavior was also verified by non-Gaussian negativity of Wigner function. Our hybrid communication model is based on temporal width- and coherence time-contrast, which can be controlled by wavelength (power) of input beams. The coherence time-contrast is about 90%.

1. INTRODUCTION

The rapid development of hybrid quantum systems, in which some quantum system effectively become classical, holds a great significance for the foundation of quantum optics [1]. As part of this ongoing effort, devices for quantum information processing, secure communication, and high-precision sensing are being implemented with diverse and hybrid systems, ranging from photons, atoms, and spins [2]. Photons are well suited for transmitting quantum information, especially in a hybrid state of entanglement and qubits [3,4]. The potential objective of hybrid quantum technologies is to develop devices that can simultaneously perform several tasks, such as reliably store, process, and transmit quantum or classical information [5]. Hybrid entangled states are becoming important tools for converting quantum information between different formats and encodings to optimize its transmission, manipulation, and storage [6] while maximizing the fidelity [7]. Non-classical signals usually achieve high fidelities but at the expense of hard-to-scale probabilistic implementations. With such a complementary approach of different physical systems, hybrid entanglement, [4] crossover of both classical and quantum state [8] and hybrid tripartite telecom photons [9] have become of special interest as complementary building blocks for hybrid quantum technologies and systems [5,10].

Redman et al. investigated spin dynamics and electronic states of diamond NV centers using electron paramagnetic resonance and FWM spectroscopy [11]. Raman-excited spin coherences and Raman heterodyne detection nuclear magnetic resonance signals associated with hyperfine transitions in diamond NV center are extensively reported [12,13]. In this article, we realized an optical multi-channel hybrid communication system from a negatively charged diamond Nitrogen–vacancy center (NV^-) [14,15]. We configured NV center using spontaneous parametric four-wave mixing (SP-FWM). For one-channel hybrid communication, we generated a composite signal of fluorescence (FL) and Stokes ($\boldsymbol{E}_S$) of broad temporal width from off-resonant beam that is sent from transmitter to receiver. For the recovery of the FL signal at the receiver end, coherent signal ($\boldsymbol{E}_S$ and anti-Stokes ($\boldsymbol{E}_{AS}$)) is generated from a coherent oscillator using resonant excitation, which acts as a reference signal at the demodulator. Later, we extend this idea to two-mode and three-mode intensity–noise correlation to realize two-channel and three-channel hybrid communication, respectively. The multi-order FL correlate because of nonlinear interaction regulated by dressing effects, while the quantum correlation is based on third-order nonlinear interaction in the system. For multi-channel hybrid communication, we devised a scheme to generate hybrid entangled

* Corresponding authors.
E-mail addresses: iahmed8-c@my.cityu.edu.hk (I. Ahmed), ypzhang@mail.xjtu.edu.cn (Y. Zhang).

https://doi.org/10.1016/j.optcom.2021.127073
Received 10 February 2021; Received in revised form 26 April 2021; Accepted 28 April 2021
Available online 1 May 2021

states by subtracting a single photon from composite signal through beam splitter of low reflectivity. Hybrid signal is cross correlated with $\boldsymbol{E}_{\mathrm{AS}}$, who is corresponding to squeezing (−5 dB) and correlation value (1.1) violates Cauchy–Schwarz inequality. Such nonclassical behavior was theoretically verified through non-Gaussian negativity of the Wigner function of the hybrid signal. Our experimental results provide the advance technique of coherence time contrast and channel index of about 90% applicable to multi-channel hybrid communication.

2. Basic theory for one-channel hybrid communication

The sample used in our experiment is a bulk NV$^-$ center crystal synthesized by chemical vapor deposition (the surfaces had sizes of 4.5 mm ×4.5 mm with a thickness of 0.3 mm), consisting of substitutional nitrogen–lattice vacancy pairs orientated along the ⟨100⟩ crystalline direction. The sample was doped with nitrogen with a concentration of less than five parts per billion (ppb) and typically had less than 0.03 ppb NV center concentration. The sample in a cryostat was maintained at 77 K by flowing liquid nitrogen to overcome the zero field splitting [16]. Fig. 1(a) is a schematic diagram of the experimental setup. Two tunable dye lasers (narrow scan with a 0.04 cm^{-1} linewidth) pumped by an injection-locked single-mode Nd:YAG laser (Continuum Powerlite DLS 9010, 10 Hz repetition rate, 5 ns pulse width) are used to generate the pumping fields $\boldsymbol{E}_1$ (ω_1, Δ_1) and $\boldsymbol{E}_2$ (ω_2, Δ_2) with frequency detuning $\Delta_{\mathrm{i}} = \Omega_{\mathrm{mn}} - \omega_{\mathrm{i}}$, where Ω_{mn} is the corresponding atomic transition frequency between levels $|\mathrm{m}\rangle$ and $|\mathrm{n}\rangle$, ω_{i} (i=1,2) is the laser frequency. The diameter of all input beams is 0.1 mm, and their polarization is controlled by inserting wave plates into their respective beam paths. The diamond NV$^-$ center has two triplet states, named ground state $^3\mathrm{A}_2$ and excited state $^3\mathrm{E}$, and two singlet states ($^1\mathrm{A}_1$, $^1\mathrm{E}$). The two triplet states $^3\mathrm{A}_2$ and $^3\mathrm{E}$ split into $|\mathrm{m_s}=0\rangle$ and $|\mathrm{m_s}=\pm1\rangle$ fine-structure levels. The energy difference between $|\mathrm{m_s}=0\rangle$ and $|\mathrm{m_s}=\pm1\rangle$ for $^3\mathrm{A}_2$ is D = 2.8 GHz [15] while for excited state $^3\mathrm{E}$ D = 1.42 GHz. At low temperature, orbit–orbit and spin–spin interaction split the excited state triplet into four levels i.e.

$|\mathrm{A}_2, \mathrm{m_s}=\pm1\rangle$, $|\mathrm{A}_1, \mathrm{m_s}=\pm1\rangle$, $|\mathrm{E}_{1,2}, \mathrm{m_s}=\pm1\rangle$ and $|\mathrm{E}_{x,y}, \mathrm{m_s}=0\rangle$, three of which are degenerate. The spin of the $E_{x,y}$ states is $m_s = 0$ as shown in Fig. 1(b). All others states are superpositions of $|\mathrm{m_s}=+1\rangle$ and $|\mathrm{m_s}=-1\rangle$. The transitions between the ground state and the excited state are in the visible and follow the selection rules given [17]. At low temperature they can be resonantly excited using a laser of the corresponding frequency and this way different spin states can be selectively addressed. The dressed energy levels $|\pm\rangle$ are shown in Fig. 1(g).

2.1. SPFWM modeling at the receiver

Fig. 1(b) shows the energy level scheme of the diamond NV$^-$ center. In the current experiment, the SPFWM process occurs via a self-diffraction-type FWM process in which $\boldsymbol{E}_S$ (ω_S) and $\boldsymbol{E}_{AS}$ (ω_{AS}) are generated by absorbing pump photons ω_2 and a control photons ω_2 as shown in Fig. 1(c).

The emitted signals $\boldsymbol{E}_{\mathrm{S}}$ and $\boldsymbol{E}_{\mathrm{AS}}$ form a conical spatial alignment and can only be detected in a particular direction that satisfy phase matching $\boldsymbol{k}_2 + \boldsymbol{k}_2 = \boldsymbol{k}_{\mathrm{S}} + \boldsymbol{k}_{\mathrm{AS}}$ and energy conservation, $\hbar\omega_1 + \hbar\omega_2 = \hbar\omega_S + \hbar\omega_{AS}$ condition, where ω_S and ω_{AS} are the frequency tuning for Stokes and anti-Stokes photon, respectively. Such process is also referred as conditional two-photon sources. Photomultiplier tubes (PMT), PMT1 and PMT2 are precisely placed to detect composite (FL+$\boldsymbol{E}_{\mathrm{S}}$) and anti-Stokes ($\boldsymbol{E}_{\mathrm{AS}}$) signals, respectively. FL has random direction and vanishes before reaching PMT2. Therefore, PMT3 is placed near to NV$^-$ center to collect the pure FL signal. Since the FL and SPFWM have different buildup times and decay rates, therefore can be easily distinguished at any PMT using boxcar gate position. If the gate width is narrow (100 ns), the observed signal comes from a single energy level with single lifetime which experiences strong dressing effect. Broad

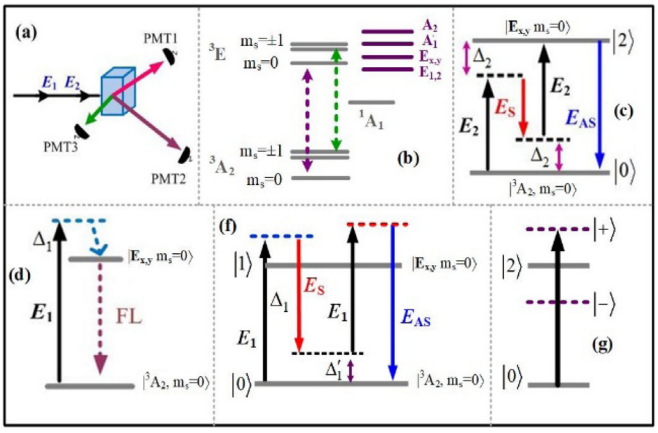

Fig. 1. (a) Schematic diagram of the experimental setup. (b) The energy level structure of NV$^-$ with triplet excited (^{3}E) and ground states (^{3}A$_2$) associated with intermediate metastable singlet state (^{1}A$_1$). (c) and (d) Two-level atomic systems in NV$^-$ center and the laser coupling configuration, respectively where $\Delta_1(\Delta_1 = \Omega_{10} - \omega_1)$ and $\Delta_2(\Delta_2 \simeq 0)$ are frequency detunings of $\boldsymbol{E}_1$ and $\boldsymbol{E}_2$ fields, respectively, PMT: photomultiplier tube; $\boldsymbol{E}_{\mathrm{S}}$: Stokes signal; $\boldsymbol{E}_{\mathrm{AS}}$: anti-Stokes signal; $|0\rangle$; ($|^3\mathrm{A}_2, \mathrm{m_s}=0\rangle$): ground-state energy level; $|1\rangle(|^3\mathrm{E}, \mathrm{m_s}=\pm1\rangle)$ and $|2\rangle$ ($|\mathrm{E}_{x,y}, \mathrm{m_s}=0\rangle$): excited-state energy levels ($|0\rangle \rightarrow |1\rangle$ = 575 nm, $|0\rangle \rightarrow |2\rangle$ = 637 nm). (f) The FWM transition paths for the Stokes ($\Delta_S = \Delta_1 - \Delta_1'$) and anti-Stokes ($\Delta_{AS} = \Delta_1 + \Delta_1'$) and anti-Stokes pair under off-resonant excitation. (g) Dressed energy level.

gate width (>1 μs) incorporates the effect of many energy levels having many lifetimes and scattering which neutralizes the dressing effect. In our experiment, we have set gate width at 100 ns. The resonant dressing beam $\boldsymbol{E}_2$ (637 nm) excites the NV$^-$ ground state $|^3\mathrm{A}_2, \mathrm{m_s}=0\rangle$ to the excited state $|\mathrm{E}_{x,y}, \mathrm{m_s}=0\rangle$, and some particles are transferred to $|^3\mathrm{E}, \mathrm{m_s}=\pm1\rangle$ due to the induced phonon effect that eventually degenerate to ground state with the FL emission. The direct transition from $|\mathrm{E}_{x,y}, \mathrm{m_s}=0\rangle$ to $|^3\mathrm{A}_2, \mathrm{m_s}=0\rangle$ in NV$^-$ is attributed as the coherent emission ($\boldsymbol{E}_{\mathrm{S}}$ and $\boldsymbol{E}_{\mathrm{AS}}$)(14, 15). It should be note that these outputs have been obtained without magnetic field. SPFWM generated from a coherent oscillator will serve the purpose of reference key required at the demodulator in our proposal shown in Fig. 2(b). Due to the dominant emission from the $|\mathrm{E}_{x,y}, \mathrm{m_s}=0\rangle$ state over the $|^3\mathrm{E}, \mathrm{m_s}=\pm1\rangle$, a resonant excitation produces very weak second-order FL emission. The dressed density matrix for $\boldsymbol{E}_{\mathrm{S}}$ and $\boldsymbol{E}_{\mathrm{AS}}$ in a two-level system ($|0\rangle \leftrightarrow |2\rangle$) via perturbation chains $\rho_{00}^{(0)} \xrightarrow{E_2} \rho_{20}^{(1)} \xrightarrow{E_{AS}} \rho_{00}^{(2)} \xrightarrow{E_2} \rho_{20(\mathrm{S})}^{(3)}$ and $\rho_{00}^{(0)} \xrightarrow{E_2} \rho_{20}^{(1)} \xrightarrow{E_S} \rho_{00}^{(2)} \xrightarrow{E_2} \rho_{20(\mathrm{AS})}^{(3)}$ are written as

$$\rho_{20(\mathrm{AS})}^{(3)} = \frac{-iG_S\mathrm{G}_2\mathrm{G}_2}{(\Gamma_{20} + i\Delta_2)(\Gamma_{00} - i\Delta_2 + |\mathrm{G}_2|^2/(\Gamma_{00} - i\Delta_2))\Gamma_{22}} \tag{1a}$$

$$\rho_{20(\mathrm{S})}^{(3)} = \frac{-iG_{\mathrm{AS}}\mathrm{G}_2\mathrm{G}_2}{(\Gamma_{20} + i\Delta_2)(\Gamma_{00} - i\Delta_2 + |\mathrm{G}_2|^2/(\Gamma_{00} - i\Delta_2))\Gamma_{22}} \tag{1b}$$

Where $G_i = \mu_{ij}E_i/\hbar$ is the Rabi frequency of $\boldsymbol{E}_{\mathrm{i}}$, μ_{ij} is the electric dipole moment between levels $|\mathrm{i}\rangle$ and $|\mathrm{j}\rangle$, and $\Gamma_{ij} = (\Gamma_i + \Gamma_j)/2$ is the transverse decay rate. The lifetime of the $\boldsymbol{E}_{\mathrm{S}}/\boldsymbol{E}_{\mathrm{AS}}$ signal is $\Gamma_{S/AS} = \Gamma_{coh} = \Gamma_{20} + \Gamma_{00} + \Gamma_{22}$. At low temperature, energy level $|2\rangle$ ($|\mathrm{E}_{x,y}, \mathrm{m_s}=0\rangle$) is splitted into dressed energy levels $|\pm\rangle$ (shown in Fig. 1(g)), the frequency tuning for ω_S and ω_{AS} photons are determined through these dressed energy levels. In frequency space, the entanglement is the result of the frequency momentum conservation, which we approximate the frequencies ω_{Si} of Stokes as small quantum deviations window δ_i around the central frequency ϖ_S. ω_S, therefore, can be written as $\omega_S = \varpi_S + \delta_1$ with the limitation of $|\delta_1| \ll \varpi_S$. Furthermore, due to the frequency correlation, the deviations windows of generated photons also satisfy $\delta_1 + \delta_2 = 0$. As a result, the Stokes and anti-Stokes share quantum entanglement. The generated Stokes and anti-stokes photon pair detected at one channel (PMT1/PMT2), their

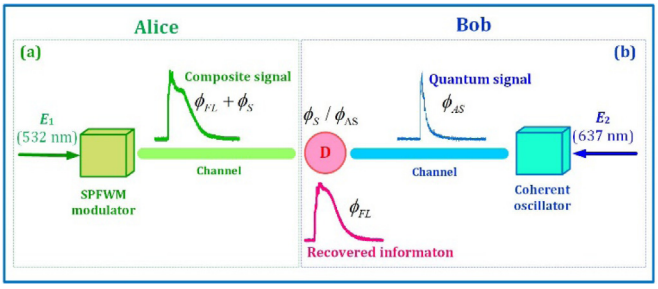

Fig. 2. One-channel hybrid communication realized model. (a) Modulator of composite signal, (b) Demodulator assisted by coherent oscillator in NV-center of diamond.

superposition can be described like the dressed energy–time superposition $\left(|\omega_{AS} + \Omega_e/2\rangle|\omega_S - \Omega_e/2\rangle - |\omega_{AS} - \Omega_e/2\rangle|\omega_S + \Omega_e/2\rangle\right)/\sqrt{2}$ [18], where $\pm\delta = -(\Delta/2) \pm \Omega_e$, $\Omega_e = \sqrt{\Delta_2^2 + 4(G_{2*}/G_2)^2\Gamma_{20}\Gamma_{00} + G_2^2}$ is effective Rabi frequency [14].

The temporal intensity of the E_S/E_{AS} signals is $I_{S/AS} = \rho^{(3)}_{S/AS} \exp(-\Gamma_{S/AS}t)$. The coupling Hamiltonian for the SPFWM process is $H = (\hat{a}^\dagger_S \hat{a}^\dagger_{AS} + \hat{a}_S \hat{a}_{AS})g/v$, where $\hat{a}^\dagger_S(\hat{a}_S)$ and $\hat{a}^\dagger_{AS}(\hat{a}_{AS})$ are creation and annihilation operators are acting on Stokes and anti-Stokes signals, respectively, while v is group velocity of the field in the nonlinear medium. The nonlinear gain $g = \left|(-i\omega_{S,AS}\chi^{(3)}_{S,AS}E_1E_2/2c)\right|$ depends on the nonlinear susceptibility $\chi^{(3)}_{S,AS} = \left(N\mu_{S,AS}\rho^{(3)}_{S,AS}\right)/\left(\varepsilon_0 E_1 E_2 E_{S,AS}\right)$ and the pumping field amplitude. Based on the above Hamiltonian, the propagation dynamics is as follows

$$da_S/dt = \chi^{(3)}_S a^+_{AS} \exp(i\varphi_S) \tag{2a}$$

$$da_{AS}/dt = \chi^{(3)}_{AS} a^+_S \exp(i\varphi_{AS}) \tag{2b}$$

In the above equation $\varphi_S/_{AS}$ is E_S/E_{AS} phase. Thus, the Stokes and anti-Stokes intensities are proportional to the respective photon number $(N_j = \langle \hat{a}^+_j \hat{a}_j \rangle)$ as

$$\langle \hat{a}^+_S \hat{a}_S \rangle = \frac{1}{2}\left[\cos(2t\sqrt{AB}\sin\frac{\varphi_1+\varphi_2}{2}) + \cosh(2t\sqrt{AB}\cos\frac{\varphi_1+\varphi_2}{2})\right]\frac{A}{B} \tag{3a}$$

$$\langle \hat{a}^+_{AS} \hat{a}_{AS} \rangle = \frac{1}{2}\left[\cos(2t\sqrt{AB}\sin\frac{\varphi_1+\varphi_2}{2}) + \cosh(2t\sqrt{AB}\cos\frac{\varphi_1+\varphi_2}{2})\right]\frac{B}{A} \tag{3b}$$

where the substitutions of $\rho^{(2)}_S = Ae^{i\phi_1}$ and $\rho^{(3)}_{AS} = Be^{i\phi_2}$ are taken from Eqs. (1a) and (1b). In above equations A(B) are the modulus and ϕ_1/ϕ_2 are the phase angles of $\rho^{(3)}_S(\rho^{(3)}_{AS})$, respectively, and t is time. Similarly, the phase for FL can be written as $\rho^{(2)}_{FL} = Ce^{i\phi_{FL}}$.

2.2. Composite signal modeling at the transmitter

When the diamond NV$^-$ center is excited with off-resonant E_1 (532 nm) beam, the composite signal containing E_S and FL signal is generated(20–22). In a two-type level system ($|0\rangle \leftrightarrow |1\rangle$) shown in Fig. 1(d), FL via perturbation chain $\rho^{(0)}_{00} \xrightarrow{E_1} \rho^{(1)}_{10} \xrightarrow{E^*_1} \rho^{(2)}_{11}$ is written as

$$\rho^{(2)}_{11} = \frac{-G_1^2}{(\Gamma_{10} + i\Delta_1)\Gamma_{11}} \tag{4}$$

Lifetime of FL is $\Gamma_{FL} = \Gamma_{10} + \Gamma_{11}$. The temporal intensity of FL is $I_{FL} = \rho^{(2)}_{FL} \exp(-\Gamma_{FL}t)$. Due to the effect of off-resonant excitation, high phonon induced mixing caused by laser heating results in high phonon induced dipole-allowed transitions to $|^3E, m_s = \pm1\rangle$ from $^3A_2$ which results in significant dominance of FL emission over E_S. In this experiment, coherent signals (Stokes/anti-Stokes) were generated from the SPFWM process, and incoherent (composite FL+E_S) signal were obtained from cross-Kerr nonlinear interaction. To generate the composite signal, we used a scheme similar to the one explained in [19], where the cross-Kerr nonlinearity coefficients are responsible for the interaction of the E_S and FL signals in the nonlinear crystal. Cross-Kerr nonlinearity is essential for the generation of an entangled state. The Kerr nonlinearity is characterized by a refractive index $n_0 + n_2|E|^2$, where n_0 is the weak-field linear refractive index term and $n_2 = 3\chi^{(3)}/2n_0$ is a nonlinear refractive index. Because of the coherence of the nonlinear medium, the interaction between the SPFWM and FL outputs results in a composite signal. This nonlinear interaction is attributed to combination of a common energy level, a strong pumping field, a dressing field and propagation through a common medium, thus creates such an interaction between the generated coherent SPFWM signals and the FL. This effect also allows to create superposition of two unique states [4,20]. Therefore, composite signal and Stokes are cross-correlated. The superposition of the coherent SPFWM state ($\pm\delta$) and incoherent FL state (ω_α) can be written as $|\Psi_1\rangle = [|\omega_S - \delta\rangle|\omega_\alpha\rangle + |\omega_S + \delta\rangle|-\omega_\alpha\rangle]/\sqrt{2}$, where ω_α is the frequency of multi-order FL. Our hybrid entanglement is superposition of coherent and multi-order FL (ω_α). It should be noted that multi-order FL comes from nonlinear interaction caused by Kerr nonlinear coefficients having components of both SPFWM and FL. Due to the classical properties of incoherent states, $|\Psi_1\rangle$ state can be considered as the optical implementation of Schrodinger's cat Gedanken experiment [21], as it manifests the entanglement between quantum and classical states. This composite signal is further realized as a modulated signal, in which FL is riding as information on the carrier (E_S) signal, making classical and coherent superposition. In this proposed modulation, linewidth of FL is almost ten times greater than the linewidth of coherent signal, satisfying the modulation law. At receiver of one-channel hybrid communication, the phase of the composite signal ($\phi_S + \phi_{FL}$) is matched with the phase of reference $E_{AS}(\phi_{AS})$ generated from a coherent oscillator at a demodulator (ϕ_S/ϕ_{AS}) to recover information signal. At demodulator, in-phase E_S and E_{AS} signals (initial relative phase between E_S and E_{AS} is ($\Delta\varphi_I \approx 0$) cancel each other and out-of-phase FL emission (initial relative phase between E_S/E_{AS} and FL is ($\Delta\varphi_I \approx \pi$) can be recovered as information signal through one-mode homodyne detection. In our experiment setup, by subtracting intensities of composite signal detected at PMT1 (Fig. 3(a)) from E_{AS} from coherent oscillator (PMT2), intensity information FL signal (similar to FL signal detected at PMT3) is recovered at receiver's end (Fig. 3(b)). In comparison to off-resonant excitation (532 nm), resonant beam (637 nm) can excite coherent oscillators efficiently due to strong SPFWM emission, as shown in Fig. 3(b).

2.3. Results of one-channel hybrid communication

Figs. 3(a1)–3(a3) shows the time domain intensity of composite signal detected at PMT1 as power (P_1) of off-resonant beam E_1 (532 nm) increases from 1 mW to 3 mW. Two peaks emerging sequentially (sharp followed by broad peak) are associated with the composite signal in Fig. 3(a1). The sharp peak (E_S) comes from the population transfer between states $|^3A_2, m_s = 0\rangle$ to $|E_{x,y}, m_s = 0\rangle$ while broad peak (FL) results from phonon induced dipole-assisted transition to $|^3E, m_s = \pm1\rangle$ from $^3A_2$. The intensity of E_S and FL signal is related to density matrix elements as $I_{S/AS} \propto |\rho^{(3)}_{S/AS}|^2$ and $I_{FL} \propto |\rho^{(2)}_{11}|^2$, respectively. Since the generation and detection are simultaneous, therefore recorded the intensity of this modulated output is $I_{FL} + I_S$ $(|\rho^{(2)}_{11}|^2 + |\rho^{(3)}_{S/AS}|^2)$. As power P_1 changes from 1 mW (Fig. 3(a1)) to 3 mW (Fig. 3(a3)), population transfer mostly happens to $|^3E, m_s = \pm1\rangle$ because of phonon induced effect. Due to the excitation of E_1 at high power, high phonon-induced mixing caused by strong laser heating results in the domination of population transfer from $|^3E, m_s = \pm1\rangle$. Hence, FL emission $\rho^{(2)}_{11}$ dominates over coherent Stokes $\rho^{(3)}_S$ in the composite signal, and the pure broad peak is observed (Fig. 3(a3)). Fig. 3(b) shows the time

domain intensity of pure E_{AS} (detected at PMT2) obtained by exciting NV^- from resonant dressing beam E_2 (637 nm) when P_2 is changed from 1 mW to 3 mW. At low power, the sharp peak is more obvious due to strong coherent emission $\rho^{(3)}_{10(S)}$(Fig. 3(b1)). When P_2 is increased to high, the intensity of coherent emission $I_S \propto |\rho^{(3)}_S|^2$ is decreased (Fig. 3(b3)) as the dressing effect $|G_2|^2/(\Gamma_{00} - i\Delta_2)$ (mentioned in Eq. (1a)) increases. By considering the dressing and phonon effect, the modified decay rate [22,23] of the $|i\rangle$ and $|j\rangle$ energy level is defined as $\Gamma_{i/j} = \Gamma_{pop} + \Gamma_{ion\text{–}spin} + \Gamma_{ion\text{–}ion} + \Gamma_{phonon} - \Gamma_{dressing}$. Where $\Gamma_{pop} = (2\pi T_1)^{-1}$ depends on the location of the energy level in phase space, with T_1 describing the population decay time, and the term $\Gamma_{dressing}$ represents the location of the energy level, which can be dressed by the coupling field. $\Gamma_{ion\text{–}spin}$ is the ion–spin coupling effect of the individual ion, $\Gamma_{ion\text{–}ion}$ is determined by the interaction among the rare-earth ions and can be controlled by the power of the external field and impurity concentration and Γ_{phonon} is related to the sample temperature. The last three terms ($\Gamma_{ion\text{–}spin} + \Gamma_{ion\text{–}ion} + \Gamma_{phonon}$) are components of $(2\pi T_2^*)^{-1}$. (the reversible transverse relaxation time T_2^*). The lifetime of a composite and coherent signal is calculated using the off-diagonal decoherence rate as 0.9 and 13 μs, respectively [24]. Under resonant excitation at low temperature, dressing effect ($\Gamma_{dressing}$) becomes strong and phonon effect (Γ_{phonon}) reduces which restricts the decay rate to low. Dressing is an effective tool to reduce decay rate and enhance lifetime. As lifetime is inversely proportional to decay rate, hence, we can conclude that lifetime increases due to increase in dressing effect in atomic-like media [25,26]. Also, we can limit the effect of large inhomogeneous broadening and often non zero ZFS by addressing single spin energy level and dressing effect.

The one-channel hybrid communication model illustrated in Fig. 2 is realized from the time domain intensity results observed in Fig. 3. The composite signal (FL+E_S) is sent from the transmitter to the receiver. At the receiver end, the information signal (FL) is recovered through E_{AS} generated from a coherent oscillator, which serves as a reference key for the demodulator (Fig. 2(b)). Temporal width contrast compares linewidth of composite signal (Δt_{com}) generated at transmitter end with coherent signal (Δt_{coh}) generated at the receiver end. Temporal width contrast ($C_t = \Delta t_{com}/\Delta t_{coh}$) of demodulator is measured at $C_t = 70\%$ at high power (Fig. 3(a3), 3(b3)) is associated with different lifetime and decay rates. This high value of temporal width contrast can be explained from the enhancement of FL emission (broad peak) at high power due to high phonon density with a lifetime of the composite signal. Intensity contrast ($C_1 = I_{com}/I_{coh}$) of the demodulator is the ratio of the amplitude of a composite signal (I_{com}) to the amplitude of a coherent signal (I_{coh}). In our experiment, C_1 increases from 0.8 (Fig. 3(a1), 3(b1)) to 1.2 (Fig. 3(a3), 3(b3)). In principle, $C_1 = 1.2$ suggests the over modulation, which comes from the large amplitude of a composite signal, which mainly contains more amplitude FL and less coherent signal at high power. The demodulator speed is about 20 ns and can further be controlled by the E_2 dressing field of Eq. (1).

3. TWO- AND THREE-CHANNEL HYBRID COMMUNICATION

Fig. 4(a) shows the proposed conditional setup for two-channel and three-channel hybrid communication using hybrid signal, E_{AS} and FL. In the proposed scheme (Fig. 4(a1)), PMT1, PMT2, and PMT3 detect hybrid signal, pure E_{AS}, and pure FL, respectively, and their position is same as illustrated in Fig. 1(a). A hybrid signal can be obtained by projecting a composite signal on a non-polarizing beam splitter (BS) with a very low reflection coefficient. The avalanche photodiode (APD) and PMT1 are placed to detect reflection and transmission signals from BS, respectively (Fig. 4(a1)). Beam splitter with low reflection coefficient suggest similar phenomenon of subtracting a single photon from composite signal and produce a hybrid signal satisfying Wigner function [25]. In our case, Fig. 4(b2) shows a non-Gaussian negativity

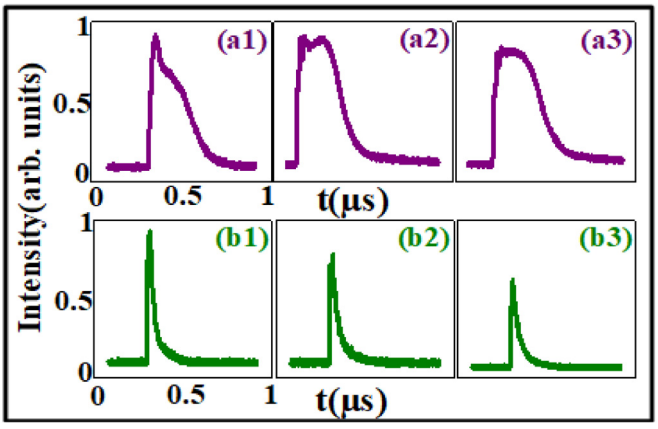

Fig. 3. The measured time-domain intensity signal from NV^- center in a two-level atomic system. (a) Composite (FL+E_S) signal and (b) Coherent (E_{AS}) signal obtained by exciting off-resonant and resonant beam, respectively.

and peak of Wigner function which corresponds to quantum and classical behavior of our hybrid signal, respectively. The hybrid entangled state $|\Psi_2\rangle$ derived from $|\Psi_1\rangle$ can be written as

$$|\Psi_2\rangle = \frac{1}{\sqrt{2}}|N_s - 1\rangle[|\alpha\rangle + |-\alpha\rangle] + \frac{1}{\sqrt{2}}|N_s\rangle[|\alpha - 1\rangle + |-\alpha - 1\rangle] \tag{5}$$

Where N_s is the number of Stokes photons and α is the photon number of multi-order FL, that can be related to second- and fourth-order FL as discussed in [27]. By applying a similar approach, we can generate entangled state $|\Psi_3\rangle$ from pure FL emission (detected at PMT3 in Fig. 4(a1)) which can be written as $|\Psi_3\rangle = \frac{1}{\sqrt{2}}|\alpha - 1\rangle + \frac{1}{\sqrt{2}}|-\alpha - 1\rangle$. Wigner function for $|\Psi_3\rangle$ would satisfy non-Gaussian negativity (Fig. 4(b2)). For two-channel and three-channel hybrid communication, phase information can be recovered through two-mode and three-mode homodyne detection, respectively [4,5]. Similar to Fig. 2, SPFWM will serve as a coherent oscillator to provide distribution key (E_{AS}) to complete hybrid communication. Two-channel (Fig. 5) and three-channel (Fig. 6) hybrid communication can be achieved through two-mode and three-mode intensity–noise correlation (squeezing), respectively.

The two-mode intensity–noise correlation function $G^{(2)}(\tau)$ between two intensity fluctuations of two optical beams as a function of time delay τ is given by [26].

$$\begin{aligned} G^{(2)}_{ij}(\tau) &= \frac{\langle \delta\hat{I}_i(t_i)\delta\hat{I}_j(t_j)\rangle}{\sqrt{\langle[\delta\hat{I}_i(t_i)]^2\rangle\langle[\delta\hat{I}_j(t_j)]^2\rangle}} \\ &= [|R_E Rc|^2 e^{-2\Gamma^+_{i/j}|\tau|} + e^{-2\Gamma^-_{i/j}|\tau|} \\ &\quad -2\cos(\Omega_e|\tau|)e^{(\Gamma^+_{i/j}+\Gamma^-_{i/j})|\tau|}] \end{aligned} \tag{6}$$

Where R_E and Rc are constants. The line shape is primarily affected by the decay rate Γ. Correlation function defined above includes effect of decay rate which can also be controlled through dressing and phonon effect. The generalized extension of Eq. (6) for three-mode $G^{(3)}(\tau_1, \tau_2, \tau_3)$ is

$$\begin{aligned} G^{(3)}(\tau_1, \tau_2, \tau_3) &= \frac{\langle \delta\hat{I}_1(t_1)\delta\hat{I}_2(t_2)\delta\hat{I}_3(t_3)\rangle}{\sqrt{\langle[\delta\hat{I}_1(t_1)]^2\rangle\langle[\delta\hat{I}_2(t_2)]^2\rangle\langle[\delta\hat{I}_3(t_3)]^2\rangle}} \\ &= C\int d\omega_2 \left| e^{-\omega_2 t_3}\frac{\kappa_1\kappa_2\sinh^2(\Omega L)\cosh(\Omega L)}{\Omega^2}\right|^2 \\ &\quad -D\int d\omega_2 \left| e^{-\omega_2(t_2-t_1)}\frac{\kappa_1\kappa_2\sinh^2(\Omega L)\cosh(\Omega L)}{\Omega}\right| \end{aligned} \tag{7}$$

Similarly, the degree of two-mode intensity-difference squeezing is given by [28]

$$Sq^{(2)}_{ij} = Log_{10}\frac{\langle\delta^2(\hat{I}_i - \hat{I}_j)\rangle}{\langle\delta^2(\hat{I}_i + \hat{I}_j)\rangle} \tag{8}$$

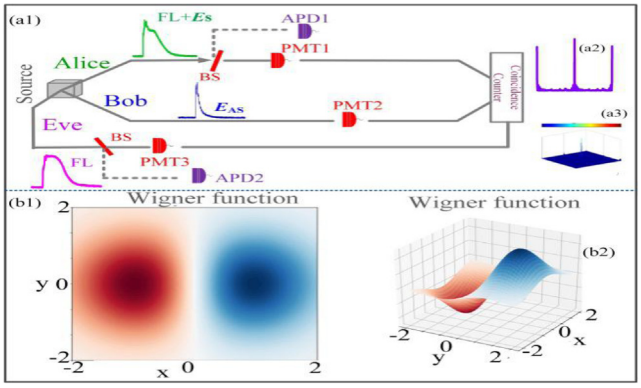

Fig. 4. (a) Proposed method for hybrid communication in diamond NV⁻ center using noise-correlation and squeezing. (a1) and (a2) two- and three-mode intensity–noise correlation, respectively, APD: avalanche photodiode. (b2) Calculated Wigner function for the non-Gaussian negativity of hybrid entangled state, (b1) is projection of (b2).

Where $\langle\delta^2(\hat{I}_i - \hat{I}_j)\rangle$ is the mean square deviation of the intensity-difference and $\langle\delta^2(\hat{I}_i + \hat{I}_j)\rangle$ is the mean square deviation of the intensity sum of the coherent laser beams.

3.1. Two-mode intensity–noise correlation

In Fig. 5(a), we investigated the two-mode intensity–noise correlation of FL and hybrid (H_1=FL+E_S), where H_1 is hybrid signal obtained under off-resonant excitation) signals by changing the power of E_1 (532 nm) from low (1 mW) to high (4 mW). In Fig. 5(a), for measuring two-mode correlation, we blocked the PMT2 and kept the rest of the PMTs on scanning mode (from Fig. 4(a1)). The time-dependent intensity fluctuations of the FL signal ($\delta\hat{I}_{FL}(t_{FL})$) from PMT3 and hybrid signal ($\delta\hat{I}_{H_1}(t_{H_1})$) from PMT1 are plotted using $G^{(2)}_{H_1-FL}$ (Eq. (6)). As P_1 is set to 1 mW, the proportion of E_S in the hybrid signal is slightly in high proportion.

With this proportion, there is little phase similarity between the hybrid and the FL signal, so the amplitude of correlation is low as shown in Fig. 5(a1). At high power, phonon-induced dipole-assisted transitions between ground-excited states increases significantly due to the strong gain effect of $|G_1|^2$, hybrid signal behaves more like pure FL signal with very less proportion of coherent emission. When P_1 approaches 4 mW, the intensity of the hybrid signal increases so is the amplitude of correlation in Fig. 5(a4), which is also reinforced by a similar phase between hybrid and FL at high power. Due to the reduction of E_S proportion in a hybrid signal at high power, the coherence time of $G^{(2)}_{H_1-FL}$ decreases, which causes lineshape of the correlation curve to become more sharp (Fig. 5(a4)). Fig. 5(b1)–5(b3) show two-mode correlation ($G^{(2)}_{H_2-AS}$) between E_{AS} and hybrid (H_2=FL+E_S, where H_2 is hybrid signal obtained under resonant excitation) signals detected at PMT2 and PMT1, respectively, when NV⁻ center is excited by resonant beam E_2 (637 nm). When the power of E_2 is kept low (1 mW), the population transfer between $|^3A_2, m_s = 0\rangle$ and $|E_{x,y}, m_s = 0\rangle$ is high resulting in strong coherent emission $\rho^{(3)}_{20(S)}$. As observed in Fig. 3(b1), phonon-induced transitions (FL emission) is almost negligible when power of resonant beam is kept at 1 mW. Hence, at low power, E_S in hybrid signal significantly dominates over FL emission and hybrid signal behaves like a pure E_S signal. Since, Stokes and anti-Stokes photons are produced under phase matching ($k_2 + k_2 = k_S + k_{AS}$) and energy conservation ($\omega_2 + \omega_2 = \omega_S + \omega_{AS}$, where ω is transition frequency) condition based on dressing and energy–time entangled state, hence, hence, high amplitude of correlation is observed in Fig. 5(b1). Now, we use the Cauchy–Schwarz inequality $G^{(2)}_{H_2-AS} \leq 1$ to check our experimental result (Fig. 5(b1)). The measured correlation at off resonance is about 1.1, which clearly violates of the Cauchy–Schwarz inequality, proving that there is a nonclassical

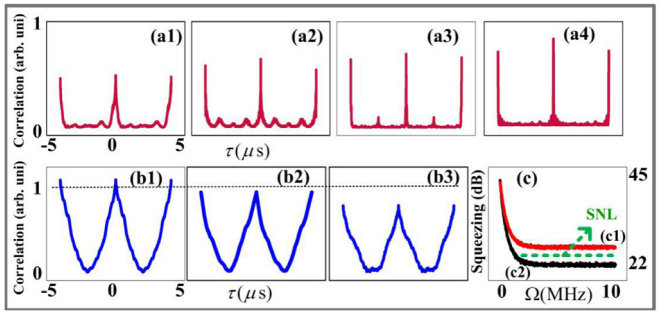

Fig. 5. (a1)–(a4). show two-mode intensity–noise correlation between FL and hybrid signal (H_1=FL+E_S) by changing power of E_1 (532 nm) from 1 mW (left) to 4 mW (right); (b1)–(b3) hybrid (H_2=FL+E_S) signals and E_{AS} by changing power of E_2 (637 nm) from 1 mW to 3 mW.

correlation between E_S and E_{AS} and reinforced by measured squeezing of −5 dB (Fig. 5(c)). When power of E_2 is increased from 1 mW to 3 mW, intensity of $E_S(I_S \propto \rho^{(3)}_{20(S)})$ is decreased and proportion of FL emission in hybrid signal slightly increases due to phonon induced transition and increase in gain effect at high power as shown Fig. 3(b3). With increase in FL emission, amplitude of correlation decreases as shown in Fig. 5(b3). Correlation observed in Fig. 5(b3) does not violates Cauchy–Schwarz inequality, hence, classical correlation is observed at high power. Spectral linewidth of coherent signals is determined by the atomic coherence time and are thus much narrower corresponding to broad peak correlation throughout Fig. 5(b).

The shot noise level (SNL) (dashed curve in Fig. 5(c)) for the SPFWM process is the intensity-difference squeezing on a pair of equal power beams produced from a coherent laser by a beam splitter with equal power as the sum of hybrid and anti-Stokes. The squeezing $Sq^{(2)}_{S-AS}$ in Eq. (8) is measured at −5 db. The non-classical behavior of correlation is also illustrated theoretically by plotting Wigner function which clearly shows non-Gaussian negativity in Fig. 4(b2).

The two-channel hybrid communication assisted by a coherent oscillator is realized from two-mode correlation results observed in Fig. 5. Here, channel index (C_2) of two-channel hybrid communication can be defined by $C_2 = (|G^{(2)}_{max}| - |G^{(2)}_{min}|)/(|G^{(2)}_{max}| + |G^{(2)}_{min}|)$ (where $|G^{(2)}_{max}|$ and $|G^{(2)}_{min}|$ are maximum and minimum amplitudes of correlation, respectively) is analogous to signal to noise ratio of the information signal. When C_2 is approaching 100%; we will have less noise and recover more information accurately. Here the channel index can approach maximum up to $C_2 = 91\%$ for $G^{(2)}_{H_1-FL}$ (Fig. 5(a3)) and 95% for $G^{(2)}_{H_2-AS}$ (Fig. 5(b1). The coherence time contrast (C_{τ_1}) of two-channel hybrid communication compares coherence time of $G^{(2)}_{H_2-AS}$ with $G^{(2)}_{H_1-FL}$ is defined as $C_{\tau_1} = \Delta\tau_{H_2-AS}/\Delta\tau_{H_1-FL}$. From our experiment, $C_{\tau_1} = 80\%$ (line shape of coherent correlation is found to be 80% broader than incoherent correlation) at low power in Fig. 5(a1), 5(b1), which is due to a higher lifetime and faster decaying of SPFWM (lower Γ) corresponds to a broad line shape of the correlation function. The support for these ideas came from the properties of hybrid entanglement between a single photon and a coherent state in a free-traveling field [4,29], which can be coupled to those channels such as nanophotonic waveguide [10], efficiency approaching 98% [30,31].

3.2. Three-mode intensity–noise correlation

For the three-mode correlation, the intensity fluctuations of hybrid, E_{AS} and FL signals are recorded at PMT1, PMT2, and PMT3, respectively, and plotted using Eq. (7). Fig. 6(a) shows three-mode correlation ($G^{(3)}_{532}(\tau)$) by exciting E_1 under the same experimental conditions described for Fig. 5(a). Due to excitation from off-resonant beam E_1 (532 nm), a high intensity of pure FL signal is measured at PMT3, whereas E_{AS} emissions are weak. When the power of E_1

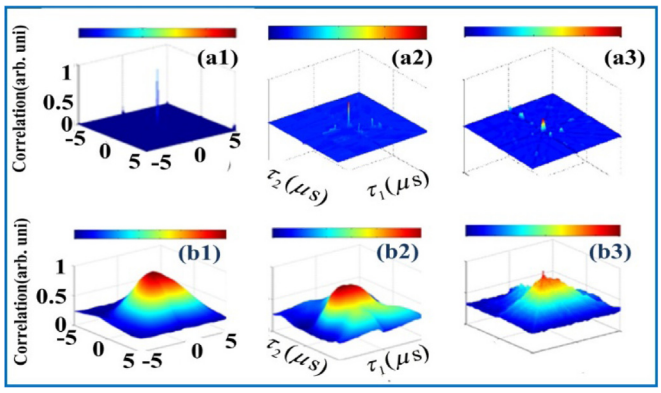

Fig. 6. Three-mode intensity–noise correlation versus delayed time between: (a1)–(a3) between hybrid signal (H_1), E_{AS} and FL by changing power of E_1 (532 nm), (b1)–(b3) between hybrid signal (H_2), E_{AS} and FL by changing power of E_2 (637 nm).

is increased, FL emission $\rho_{11}^{(2)}$ dominates Stokes $\rho_S^{(3)}$ and hybrid signal behaves as FL signal. Also, the proportion of FL detected at PMT1, and PMT3 increases significantly, whereas E_{AS} emission becomes almost negligible. At 3 mW, coherence time of $G_{532}^{(3)}(\tau)$ decreases due to increase in FL emission which results in lineshape of correlation to become extremely sharp (Fig. 6(a1)). The amplitude of $G_{532}^{(3)}(\tau)$ follow similar trend as explained in Fig. 5(a1). Fig. 6(b) show three-mode correlation ($G_{637}^{(3)}(\tau)$) by changing power of E_2 (637 nm). In the case of resonant excitation, the intensity of the FL signal detected at PMT1 and PMT3 becomes very low, and coherent emissions (E_S and E_{AS}) increases. Fig. 6(b1)–6(b3) follows a similar behavior of amplitude and shape predicted in two-mode correlation (Fig. 5(b1)–5(b3)). However, the amplitude of the three-mode correlation does not violate Cauchy–Schwarz inequality as in Fig. 6(b1). This can be explained from the effect of additional FL signal (from PMT3) in $G_{637}^{(3)}(\tau)$ as compare to $G_{H_2-AS}^{(2)}$, which prevents correlation from violating Cauchy–Schwarz inequality. By comparing Figs. 6(a) and 6(b), we can observe that lineshape of correlation signal is significantly broad under resonant excitation. This can be explained from strong E_S and E_{AS} emissions under resonant excitation, the coherence time of correlation increases, which results in broad lineshape of the correlation curve (Fig. 6(b1)).

For three-channel hybrid communication, a maximum value of coherence time contrast ($C_{\tau_1} = \Delta\tau_{G_{637}}/\Delta\tau_{G_{532}}$) is measured at about 98% (Fig. 6(a1), 6(b1)). Furthermore, the channel index $C_3 = (|G_{max}^{(3)}| - |G_{min}^{(3)}|)/(|G_{max}^{(3)}| + |G_{min}^{(3)}|)$ for three-channel hybrid communication can approach the maximum up to $C_3 = 70\%$ for $G_{532}^{(3)}(\tau)$ (Fig. 6(a3)) and 82% for $G_{637}^{(3)}(\tau)$ (Fig. 6(b1). These experimental findings suggest a physical mechanism to propose all-optical hybrid communication assisted by a coherent oscillator.

We proposed the model of hybrid communication assisted by the coherent oscillator, which may be applied to one of the building blocks of quantum communication [2,3,9,32,33] and hybrid quantum systems [10]. Further, the coherent states are non-orthogonal to each other, and they cannot be discriminated, however through our expertise of nonlinear control through cross Kerr effects, the coherent state of Stokes and anti-Stokes are distinguished through induced phase shift [34] for coherent multicarrier quadrature hybrid communication preserving the state of hybrid signal.

4. Conclusion

In summary, we realized an optical hybrid communication assisted by a coherent oscillator at low temperature by employing NV center using SP-FWM. One-channel hybrid communication action was derived by comparing time-domain intensity results of composite and coherent signals. In such a scenario, information signal is recovered from intensity difference of composite and reference coherent signals at the demodulator. Furthermore, multi-channel hybrid communication can be achieved from intensity–noise correlation where the Stokes and anti-Stokes photon pair can be described as the dressed energy–time entanglement state. Similarly, the composite signal and Stokes/anti-Stokes were cross correlated under resonant excitation, suggested non-classical behavior by violating Cauchy–Schwarz inequality (1.1) and measured squeezing (−5 dB). The superposition of such states can be maintained for few microseconds due to induced coherence. Further, a non-classical nature of correlation was calculated by non-Gaussian negativity of Wigner function. The coherence time-contrast and intensity-contrast can be controlled by power and wavelength of input beams.

CRediT authorship contribution statement

Faisal Nadeem: Writing - original draft. **Faizan Raza:** Performed the experiment. **Kangkang Li:** Performed simulation. **Huanrong Fan:** Writing - original draft. **Irfan Ahmed:** Supervised the whole study. **Changbiao Li:** Performed the experiment. **Yanpeng Zhang:** Supervised the whole study.

Declaration of competing interest

The authors declare that they have no known competing financial interests or personal relationships that could have appeared to influence the work reported in this paper.

Acknowledgments

This work was supported by the National Key R&D Program of China (2017YFA0303700, 2018YFA0307500), National Natural Science Foundation of China (61975159, 61605154, 11604256, 11804267, 11904279).

References

[1] W.H. Zurek, Decoherence, einselection, and the quantum origins of the classical, Rev. Modern Phys. 75 (2003).
[2] G. Kurizki, P. Bertet, Y. Kubo, K. Mølmer, D. Petrosyan, P. Rabl, J. Schmiedmayer, Quantum technologies with hybrid systems, Proc. Natl. Acad. Sci. U S A 112 (2015) 3866–3873.
[3] H. Jeong, A. Zavatta, M. Kang, S.W. Lee, L.S. Costanzo, S. Grandi, T.C. Ralph, M. Bellini, Generation of hybrid entanglement of light, Nat. Photon. 8 (2014) 564–569.
[4] H. Jeong, A. Zavatta, M. Kang, S.-W. Lee, L.S. Costanzo, S. Grandi, T.C. Ralph, M. Bellini, Generation of hybrid entanglement of light, Nat. Photon. 8 (2014) 564–569.
[5] T. Tufarelli, D. Girolami, R. Vasile, S. Bose, G. Adesso, Quantum resources for hybrid communication via qubit-oscillator states, Phys. Rev. A 86 (2012) 052326.
[6] U.L. Andersen, J.S. Neergaard-Nielsen, P. Van Loock, A. Furusawa, Hybrid discrete- and continuous-variable quantum information, Nat. Phys. 11 (2015) 713–719.
[7] S. Popescu, Bell's inequalities versus teleportation: What is nonlocality?, Phys. Rev. Lett. 72 (1994) 797–799.
[8] R.Z. Vered, Y. Shaked, Y. Ben-Or, M. Rosenbluh, A. Pe'Er, Classical-to-quantum transition with broadband four-wave mixing, Phys. Rev. Lett. 114 (2015) 1–6.
[9] D.-S. Ding, W. Zhang, S. Shi, Z.-Y. Zhou, Y. Li, B.-S. Shi, G.-C. Guo, Hybrid-cascaded generation of tripartite telecom photons using an atomic ensemble and a nonlinear waveguide, Optica 2 (2015) 642.
[10] D. Hallett, A.P. Foster, D.L. Hurst, B. Royall, P. Kok, E. Clarke, I.E. Itskevich, A.M. Fox, M.S. Skolnick, L.R. Wilson, Electrical control of nonlinear quantum optics in a nano-photonic waveguide, Optica 5 (644) (2018).
[11] D.A. Redman, S. Brown, R.H. Sands, S.C. Rand, Spin dynamics and electronic states of N-V centers in diamond by EPR and four-wave-mixing spectroscopy, Phys. Rev. Lett. 67 (1991) 3420–3423.
[12] N.B. Manson, X.F. He, P.T.H. Fisk, Raman heterodyne studies of the nitrogen-vacancy centre in diamond, J. Lumin. 53 (1992) 49–54.
[13] P.R. Hemmer, A.V. Turukhin, Shahriar M.S., J.A. Musser, Raman-excited spin coherences in nitrogen-vacancy color centers in diamond, Opt. Lett. 26 (361) (2001).
[14] F. Raza, A. Imran, X. Li, W. Li, Y. Li, J. Mao, Y. Zhang, Multi-mode correlation with self- and cross-Rabi oscillation in a diamond nitrogen-vacancy center, Laser Phys. Lett. 16 (2019) 055402.

[15] R. Wang, P. Pargorn, F. Raza, I. Ahmed, H. Wang, Y. Zhang, Hybrid correlation and squeezing with spontaneously generated coherence effect, Laser Phys. Lett. 15 (2018) 085401.
[16] G.Q. Liu, X. Feng, N. Wang, Q. Li, R.B. Liu, Coherent quantum control of nitrogen-vacancy center spins near 1000 kelvin, Nature Commun. 10 (2019) 1–8.
[17] J.R. Maze, A. Gali, E. Togan, Y. Chu, A. Trifonov, E.K. Lukin, M.D., Properties of nitrogen-vacancy centers in diamond: the group theoretic approach, New J. Phys. 13 (2011) 025025.
[18] D. Zhang, Y. Zhang, X. Li, D. Zhang, L. Cheng, C. Li, Y. Zhang, Generation of high-dimensional energy–time-entangled photon pairs, Phys. Rev. A 96 (2017) 053849.
[19] C.C. Gerry, Generation of optical macroscopic quantum superposition states via state reduction with a Mach–Zehnder interferometer containing a Kerr medium, Phys. Rev. A - At Mol. Opt. Phys. 59 (1999) 4095–4098.
[20] S.A. Cummer, M. Rahm, D. Schurig, One path to acoustic cloaking, New J. Phys. 9 (2007).
[21] B.E. Schrödinger, The present status of quantum MechanicsDie Naturwissenschaften, 1935.
[22] C. Li, Z. Jiang, Y. Zhang, Z. Zhang, F. Wen, H. Chen, Y. Zhang, M. Xiao, Controlled correlation and squeezing in Pr 3 + : Y 2 SiO 5 to yield correlated light beams, Phys. Rev. Appl. 7 (2017) 014023.
[23] R.W. Equall, R.L. Cone, R.M. Macfarlane, Homogeneous broadening and hyperfine structure of optical transitions in Pr 3 + : Y 2 SiO 5, Phys. Rev. B 52 (1995) 3963–3969.
[24] G.A. Khan, I. Ahmed, F. Raza, R. Wang, C. Li, Y. Zhang, Spontaneous parametric four wave mixing and fluorescence lifetime manipulation in the diamond nitrogen vacancy center, J. Opt. Soc. Amer. B 35 (2137) (2018).
[25] M. Scully, M.S. Zubairy, Quantum Optics, Cambridge University Press, 1997.
[26] G.O. Ariunbold, Y.V. Rostovtsev, V.A. Sautenkov, M.O. Scully, Intensity correlation and anti-correlations in coherently driven atomic vapor, J. Mod. Opt. 57 (2010) 1417–1427.
[27] Z. Liu, I. Ahmed, G. Abdisa, Z. Jiang, S. Fan, Hybrid three-mode correlation and squeezing in a Pr 3 + : YSO crystal, Sci. Rep. (2017) 1–12.
[28] V. Boyer, A.M. Marino, R.C. Pooser, P.D. Lett, Entangled images from four-wave mixing, Science 321 (80-) (2008) 544–547.
[29] O. Morin, K. Huang, J. Liu, H. Le Jeannic, C. Fabre, J. Laurat, Remote creation of hybrid entanglement between particle-like and wave-like optical qubits, Nat. Photon. 8 (2014) 570–574.
[30] M. Arcari, I. Söllner, A. Javadi, S. Lindskov Hansen, S. Mahmoodian, J. Liu, H. Thyrrestrup, E.H. Lee, J.D. Song, S. Stobbe, P. Lodahl, Near-unity coupling efficiency of a quantum emitter to a photonic crystal waveguide, Phys. Rev. Lett. 113 (2014) 093603.
[31] R.S. Daveau, K.C. Balram, T. Pregnolato, J. Liu, E.H. Lee, J.D. Song, V. Verma, R. Mirin, S.W. Nam, L. Midolo, S. Stobbe, K. Srinivasan, P. Lodahl, Efficient fiber-coupled single-photon source based on quantum dots in a photonic-crystal waveguide, Optica 4 (2017) 178.
[32] S.-W. Lee, H. Jeong, Near-deterministic quantum teleportation and resource-efficient quantum computation using linear optics and hybrid qubits, Phys. Rev. A 87 (2013) 022326.
[33] R.Z. Vered, Y. Shaked, Y. Ben-Or, M. Rosenbluh, A. Pe'er, Classical-to-quantum transition with broadband four-wave mixing, 2015.
[34] I. Ahmed, Z. Zhang, F. Wen, D. Zhang, C. Li, R. Wang, Y. Zhang, Switching correlation and noise level in Pr 3+ :YSO crystal via dressing nonlinear phase, Sci. Rep. (2016) 1–8.